

Structures in compressible magnetoconvection and the nature of umbral dots

C. Tian and K. Petrovay

Eötvös University, Department of Astronomy, Budapest, Pf. 32, H-1518 Hungary

Received; accepted

ABSTRACT

Context. Structures seen in idealized numerical experiments on compressible magnetoconvection in an imposed strong vertical magnetic field show important differences with respect to those detected in observations or realistic numerical simulations of sunspot umbrae.

Aims. In order to elucidate the origin of these discrepancies, here we present a series of idealized 3D compressible magnetoconvection experiments that differ from previous such experiments in several details, bringing them closer to realistic solar conditions.

Methods. An initially vertical magnetic field B_0 is imposed on a time snapshot of fully developed solar-like turbulent convection in a layer bounded by a stable layer from above. Upon relaxation to a statistically steady state, the structure of the flow field and magnetic field is examined.

Results. Instead of the vigorous granular convection (GRC) well known to take place in nonmagnetized or weakly magnetized convection, for high values of B_0 heat is transported by small-scale convection (SSC) in the form of narrow, persistent convective columns consisting of slender upflows accompanied by adjacent downflow patches, reminiscent of the “convectons” identified in earlier semi-analytic models. For moderate field strengths flux separation (FXS) is observed: isolated field-free inclusions of GRC are embedded in a strongly magnetized plasma with SSC. Between the SSC and FXS regimes, a transitional regime (F/S) is identified where convectons dynamically evolve into multiply segmented granular inclusions and back.

Conclusions. Our results are in somewhat closer agreement with observed umbral structures than earlier idealized models, as they do reproduce the strong localized, patchy downflows immediately adjacent to the narrow convective columns. Based on recent observations of umbral dots we suggest that the conditions in sunspot umbrae correspond to the newly identified F/S transitional regime.

Key words. Sun: sunspots – magnetoconvection – MHD

1. Introduction

The spectacular increase in the resolution of solar observations experienced in the past decade has resulted in unprecedentedly detailed images and movies of the small scale structures seen in sunspots. This in turn has rekindled interest in theoretical studies of magnetoconvection in order to understand the origin of these structures. This has resulted in some spectacular breakthroughs such as the first ever numerical simulation of whole sunspots (Rempel et al. 2009b; 2009a). Despite such successes, however, there are still many questions to be answered. These questions include the exact nature of umbral substructure such as umbral dots, light bridges, dark nuclei etc., and their relation to structures seen in different numerical magnetoconvection experiments.

High resolution imaging and spectropolarimetric observations with the Swedish Solar Tower (Sobotka & Hanslmeier 2005; Riethmüller et al. 2008b; Sobotka & Puschmann 2009; Ortiz et al. 2010), Hinode (Kitai et al. 2007; Riethmüller et al. 2008a; Bharti et al. 2007b, 2009; Sobotka & Jurčák 2009) and the Dunn Solar Telescope (Bharti et al. 2007a; Rimmele 2008) have shown that umbral dots (UDs) have characteristic sizes of ~ 200 km and they are mostly short-lived, the majority having lifetimes of a few times ten minutes or less. Larger UD often split or coalesce and in high resolution images dark lanes are often seen inside them. In the bright parts of UD an upflow of ~ 1 km/s has been unambiguously detected in many instances. Strong localized downflow patches have been detected on the pe-

riphery of UD. This association with up- and downflows clearly demonstrates that UD are a manifestation of magnetoconvection in the strongly magnetized, compressible umbral plasma.

1.1. Idealized models of magnetoconvection with an imposed vertical field

In the past decades, theoretical studies of magnetoconvection in a strong, vertically oriented magnetic field have gone a long way, starting from nonlinear extensions of the classic linear stability analysis of Chandrasekhar (1961). In the past decades, these studies have proceeded through the modelling of convecting magnetized Boussinesq and anelastic fluids in 2 and 3 dimensions to modelling 3D compressible magnetoconvection in a polytropically stratified atmosphere (Weiss et al. 1996, 2002). One important realization in these studies was that the spatial separation of strongly magnetized, non-convecting plasma from weakly magnetized, convective flows admits overturning convection to take place also in situations where linear theory would predict convective stability or overstability.

As the field strength is decreased starting from a value high enough to completely suppress motions, convection first sets in in the form of narrow, needle-like vertical convective columns. The horizontal scale of these structures is small compared to the natural scale of nonmagnetized convection in the same layer, so this stage is usually referred to as “small scale convection” (SSC). While these convective columns can even exist as solitary “convecton” solutions (Blanchflower 1999; Blanchflower &

Weiss 2002; Houghton & Bushby 2010), they typically appear in large numbers. The “convectons” of earlier Boussinesq models (Blanchflower 1999; Blanchflower & Weiss 2002) are vertically elongated convective cells, with upflows and adjacent downflows embedded in stagnant fluid. In later compressible experiments (Weiss et al. 1996; Houghton & Bushby 2010), however, SSC takes the form of isolated, convective upflow plumes, their mass flux being compensated by a slow, uniform sinking motion in the surrounding magnetized fluid. The plumes are persistent and immobile, though for weaker imposed field they pulsate irregularly.

With further reduction of the imposed magnetic field, a phenomenon known as *flux separation* (FXS) takes place: large isolated patches of non-magnetized, vigorously convecting fluid appear inside the strongly magnetized component where SSC is still going on. The character of the vigorous convection in field-free patches is similar to the normal granular convection (GRC) in the nonmagnetic case. Flux separation was first detected in a simulation by Tao et al. (1998); however, it seems to be a more fragile mode of magnetoconvective energy transport than the small scale convection as in simulations without full compressibility or with lower aspect ratios it is not present. Also, magnetoconvective systems show a hysteresis-like behavior where the presence or absence of flux separation is not uniquely determined by the physical parameters of the system but also depend on its history (Weiss et al. 2002).

For even lower field strengths, the strongly magnetized component becomes confined into an intermittent network of channels separating the vigorously convecting patches. Finally, with the further decrease of the imposed field the topology changes, giving way to the well known pattern of isolated magnetic flux concentrations arranged in a magnetic network-like pattern between granules (GRC).

The above described sequence, characterized as a competition between two modes of convection (small scale columnar convection vs. vigorous granular convection), suggests an interpretation of UD as the photospheric manifestation of SSC. At the same time, there are no obvious examples of flux separation in the solar photosphere, and the short lifetimes of observed UD stand in stark contrast to the persistent character of the small-scale convective columns described above.

1.2. Numerical simulations of magnetoconvection in sunspot umbrae

Models like those described above are usually called “idealized” as they aim at a systematic study of increasingly general magnetoconvective systems that are still simple enough to allow parameter studies and to be understood in relatively simple physical terms. In consequence, they do not aspire to faithfully reproduce all the physical conditions relevant for the solar photosphere; instead, they consider convection in a polytropically stratified perfect compressible fluid, with closed boundaries and fixed diffusivities.

Another approach to the problem consists in attempting to simulate conditions prevailing in the solar photosphere as realistically as possible, including radiative transfer and a realistic equation of state in a fully compressible equilibrium model (Moradi et al. 2010). An obvious drawback of this approach is that, going to the very limits of the available computing power, it is left with too few resources for systematic parametric studies. Yet these ambitious models have been quite successful in e.g. reproducing the observed penumbral fine structure. Structures readily identified with the observed umbral dots are also seen in

such simulations, as first demonstrated by Schüssler & Vögler (2006). In contrast with the small scale convective columns of idealized models, these simulated UD have finite lifetimes, and they show a characteristic “coffee bean” structure, being crossed by a dark lane along the long axis of their oval shape. Downflows are present near the end points of the dark lane. The dark lane itself is due to an optical depth effect due to the pileup of up-flowing material below a magnetic cusp above the UD. Similar UD-like structures are also seen in the full-spot simulations of Rempel et al. (2009b, 2009a).

1.3. Objectives

Despite the impressive achievements of these state of the art simulations, some differences between the detailed properties of observed and simulated umbral dots remain (cf. Bharti et al. 2010). Even more important differences remain, however, between the nature of magnetoconvective structures in idealized models on the one hand, and in observed or simulated sunspots on the other. These differences include the contrast between the observed localized patchy downflows next to UD vs. the lack thereof around small scale convective columns in experiments; the persistent character of convective columns vs. the limited lifetimes of UD; as well as the lack of clear signs of flux separation in observed or simulated sunspots.

We cannot claim a satisfactory understanding of magnetoconvection in sunspots until the origins of these differences are properly elucidated and a convincing link between convective columns and UD is forged. For this, there is a need to bridge the gap between the idealized models and the realistic simulations. As a first step in this process, in this paper we construct an idealized magnetoconvection model where, however, we relax certain constraints employed in earlier idealized models such as Weiss et al. (2002) to bring the model closer to solar conditions. Specifically

- We consider a two-layer model wherein the convectively unstable fluid is bounded by a stable layer from above.
- We use open lower boundary conditions.
- We employ a subgrid closure scheme to account for the effects of small-scale turbulent transport.
- The overall stratification chosen, while polytropic for simplicity, is selected to be reasonably similar to the actual solar case.
- Finally, we use a novel numerical scheme, the BGK-MHD scheme that is particularly well suited for the capture of near-discontinuities in the flow like the current sheets characteristic of magnetoconvection. This admits a satisfactory reproduction of structural details despite the relatively low resolution used for the computation of a larger number of cases, as needed in parametric studies.

In the simulations we first relax a convectively unstable layer of perfect gas polytropically stratified under gravity. Then, a vertical uniform magnetic field is imposed on a snapshot of the fully developed, statistically steady turbulent convection. After a statistically steady state of magnetoconvection is attained, the properties of this system are examined. We construct a series of models with different strengths of the imposed magnetic field.

Section 2 describes the setup of numerical model. Section 3 presents and discusses the results from the simulations and discusses these results, while Section 4 concludes the paper.

2. Numerical model

In the current study, the 3D BGK-MHD code developed by Tian (2010) is applied for the solution of the following resistive MHD equations under gravitational field:

$$\partial \rho / \partial t = -\nabla \cdot \rho \mathbf{v}, \quad (1)$$

$$\partial \rho \mathbf{v} / \partial t = -\nabla \cdot (\rho \mathbf{v} \mathbf{v} - \mathbf{B} \mathbf{B}) - \nabla p_{\text{tot}} + \nabla \cdot \boldsymbol{\Sigma} + \rho \mathbf{g}, \quad (2)$$

$$\begin{aligned} \partial E / \partial t = & -\nabla \cdot [(E + p_{\text{tot}}) \mathbf{v} - \mathbf{v} \cdot \boldsymbol{\Sigma} + \mathbf{F}_d - \mathbf{B} \mathbf{B} \cdot \mathbf{v} \\ & - \mathbf{B} \times \eta (\nabla \times \mathbf{B})] + \rho \mathbf{v} \cdot \mathbf{g}, \end{aligned} \quad (3)$$

$$\partial \mathbf{B} / \partial t = -\nabla \cdot (\mathbf{v} \mathbf{B} - \mathbf{B} \mathbf{v} - \eta \nabla \mathbf{B}) \quad (4)$$

where, $p_{\text{tot}} = p_g + p_m$, $E = E_i + E_m + E_k$, p_g is the gas pressure, $p_m = \frac{1}{2} \mathbf{B} \cdot \mathbf{B}$ is the magnetic pressure, E_i is the internal energy, $E_m = \frac{1}{2} \mathbf{B} \cdot \mathbf{B}$ is the magnetic energy and $E_k = \frac{1}{2} \rho v^2$ is the kinetic energy. \mathbf{g} is the gravitational acceleration, \mathbf{F}_d the diffusive heat flux, $\boldsymbol{\Sigma}$ the viscous stress tensor, η the magnetic resistivity. All the other symbols have their standard meanings. The 3D BGK-MHD code solves the non-magnetic part of the governing equations by BGK-NS solver modified due to the Lorentz force, the magnetic part by gas kinetic theory based flux-splitting method, using the particle distribution function constructed in the BGK-NS solver. The van Leer limiter is used to reconstruct the state around the interfaces of finite volumes. The solenoidality of the magnetic field ($\nabla \cdot \mathbf{B} = 0$) is ensured by the field interpolation constraint method. The code is parallelized by the MPI protocol.

2.1. Boundary conditions

Side boundaries are periodic. The upper boundary is impenetrable and stress-free and the density and internal energy are fixed:

$$\frac{\partial v_x}{\partial z} = \frac{\partial v_y}{\partial z} = v_z = \frac{\partial \rho}{\partial t} = \frac{\partial e}{\partial t} = 0. \quad (5)$$

The lower boundary is transmitting, so here only the horizontal averages of density and internal energy are fixed at their initial values while the vertical derivatives of their fluctuations are set to zero:

$$\frac{\partial \bar{v}}{\partial z} = \frac{\partial \bar{\rho}'}{\partial z} = \frac{\partial \bar{e}_i'}{\partial z} = \frac{\partial \bar{\rho}}{\partial t} = \frac{\partial \bar{e}}{\partial t} = 0 \quad (6)$$

Throughout this paper, overbar and prime denote average and fluctuating part, i.e. for a variable a we have $a = \bar{a} + a'$. Unless explicitly stated otherwise, overline denotes horizontal average.

The magnetic field is constrained to become vertical

$$B_x = B_y = \frac{\partial B_z}{\partial z} = 0, \quad (7)$$

at both the upper and lower boundaries. In this case no magnetic flux cannot be advected into or out of the computational domain by the flow.

2.2. Initial setup

Initially, the system consists two layers: an upper stable radiative layer ($1 > z > z_1$) and a lower unstable convective layer ($z_1 > z > 0$). The upper layer is subadiabatically stratified, the lower layer is slightly superadiabatic.

$$T(z) = \begin{cases} T_0[1 + Z_1(1 + z)] & \text{for } 1 > z > z_1 \\ T_1[1 + Z_2(1 + z)] & \text{for } z_1 > z > 0 \end{cases} \quad (8)$$

$$p(z) = \begin{cases} p_0(T/T_0)^{(m_1+1)} & \text{for } 1 > z > z_1 \\ p_1(T/T_1)^{(m_2+1)} & \text{for } z_1 > z > 0 \end{cases} \quad (9)$$

where Z_1 and Z_2 are the dimensionless gradients of temperature of the subadiabatic and superadiabatic layer, respectively. m_1 and m_2 are the polytropic indices for radiative and convective layer, respectively. T_0 , p_0 are the temperature and pressure at the top lid. T_1 , p_1 are the temperature and pressure at the interface between the initial stable and unstable layers, i.e.,

$$T_0 = T(z = 1) \quad T_1 = T(z_1), \quad (10)$$

$$p_0 = p(z = 1) \quad p_1 = p(z_1). \quad (11)$$

In hydrostatic equilibrium we have

$$(m_1 + 1)Z_1 = (m_2 + 1)Z_2 = |g|. \quad (12)$$

The choice of Z_1 and Z_2 determine the temperature contrast between top and bottom, and thereby, by fitting to a standard solar model, the vertical extent of our computational domain. For this reason Z is occasionally called *depth parameter* in the literature. For m_2 we choose a value below the adiabatic value that reproduces the right value of gravity acceleration according to equation (12). For Z_1 a lower value is adopted to make the top layer subadiabatic, thus convectively stable. Then m_1 can also be determined from equation (12). The specific values of these parameters are listed in Table 2.

2.3. Treatment of radiation and subgrid scale motions

Viscosity and diffusivities due to subgrid scale turbulent eddies are calculated according to the Smagorinsky model. The dynamical viscosity is given by

$$\mu = \rho(c_\mu \Delta)^2 (2\sigma : \sigma)^{1/2}, \quad (13)$$

where c_μ is an adjustable constant, usually chosen from the range 0.1–0.2. The filter width Δ is taken to be the local resolution, colon stands for tensor contract and $\sigma = \partial_i v_j + \partial_j v_i$. The turbulent heat transfer coefficient C_S and the magnetic diffusivity η are calculated as

$$C_S = \mu/\delta \quad \eta = \mu/\rho\delta_m, \quad (14)$$

where the Prandtl number δ and the magnetic Prandtl number δ_m are assumed to be constant.

For the current study, radiative transfer is considered in the diffusion approximation. The total (radiative+turbulent) diffusive heat flux is then

$$\mathbf{F}_d = -C_T \nabla T - C_S \nabla S, \quad (15)$$

where $S = C_p(\ln T - \nabla_a \ln p)$ is the specific entropy, C_p is the specific heat at constant pressure and ∇_a is the adiabatic gradient. In the stable layer, C_T is set so that radiation carries out the input energy flux. In the convection zone, C_T is very close to zero. As $C_S = \mu/\delta$ represents turbulent diffusion, it is set to zero in the stable region.

2.4. Dimensional analysis and model parameters

We nondimensionalize all variables by choosing the following basic scales.

The scale of the length, l_{scl} , is the depth of the computational domain. For the density, gas pressure and temperature, their respective values at the top boundary are chosen as the basic scales, i.e., ρ_{scl} , p_{scl} and T_{scl} . The scales for the rest of the

Table 1. Dimensional analysis.

Scale	value	unit
ρ_{scl}	1.03×10^{-6}	g/cm^3
p_{scl}	9.94×10^5	dyn/cm^2
T_{scl}	12992.6	K
l_{scl}	1.44	Mm
t_{scl}	147.22	s
v_{scl}	9.81	Km/s
B_{scl}	3534.8	G
F_{scl}	9.75×10^{11}	erg/s/cm^2

Table 2. Summary of numerical parameters.

Parameter	Definition	Value
Grids	$N_x \times N_y \times N_z$	$60 \times 60 \times 60$
Aspect ratio	$l_x : l_y : l_z$	$5 : 5 : 1$
CFL number	$\Delta x / (v + c_s) / \Delta t$	0.3
Depth after relaxation	in PSHs	3.6
SGS Prandtl number	$\delta = \mu / \kappa$	1/3
Deardorff number	c_μ in Eq. (13)	0.2
Magnetic Prandtl number	$\delta_m = \mu / (\rho \eta)$	10
Ratio of specific heat	γ	5/3
polytropic index (radiative)	m_1	2.728
polytropic index (convective)	m_2	1.485
Depth parameter (radiative)	Z_1	2
Depth parameter (convective)	Z_2	3
Initial stable-unstable interface	z_1	0.9

Table 3. Imposed magnetic field strength in the numerical runs.

Identifier	B_0/B_e
A	0.35
B	0.70
C	1.34
D	1.41
E	2.12
F	2.82
G	3.10
H	3.53

quantities can be deduced according to dimensional analysis. For instance, the scale of velocity and time are

$$v_{\text{scl}} = (p_{\text{scl}}/\rho_{\text{scl}})^{1/2} \quad t_{\text{scl}} = l_{\text{scl}}/v_{\text{scl}}, \quad (16)$$

respectively. (Note that v_{scl} is the isothermal sound speed at the top.) In the case of magnetic field strength, an extra factor of $2\pi^{1/2}$ is introduced in the unit in order to give it a more physical meaning (of thermal equipartition field strength at the top): $B_{\text{scl}} = 2\pi^{1/2} p_{\text{scl}}^{1/2}$.

Of particular importance is the scale of the input energy flux,

$$F_{\text{scl}} = p_{\text{scl}} T_{\text{scl}}^{1/2}. \quad (17)$$

As the solar radiation flux is fixed in physical units, its value in nondimensional units will depend on the value of F_{scl} , i.e. on the position of the upper boundary of our box inside the solar convective envelope. Thus, by specifying the input flux, we can approximately control the radial location of our numerical computational domain within the standard solar model.

In summary, the input energy flux, the aspect ratio and the depth of the domain determine the “geographic” parameters of

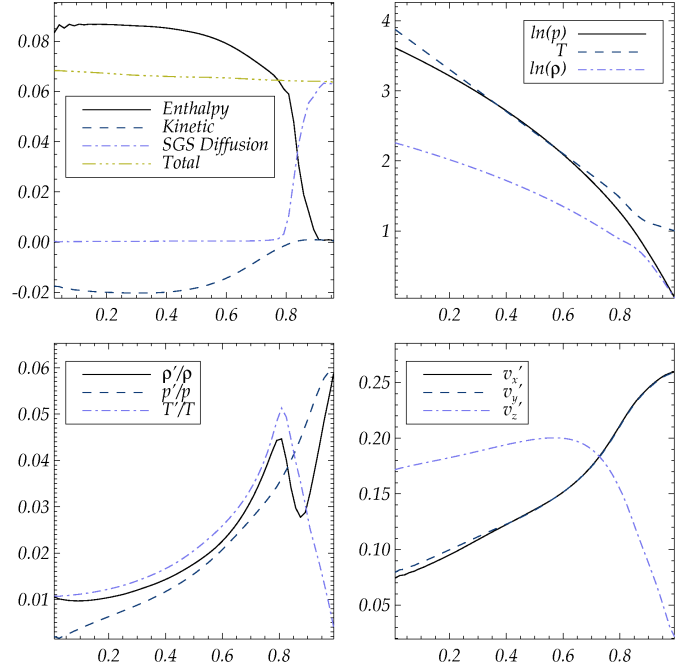


Fig. 1. Statistical properties of steady non-magnetic convection, used as initial condition for magnetoconvection. Shown are the vertical distributions of (a) contributions to the total energy flux (upper left); (b) means (lower left) and (c) rms fluctuations (lower right) of thermodynamic variables; (d) rms velocity fluctuations (lower right). Averages are taken in time and in the horizontal plane.

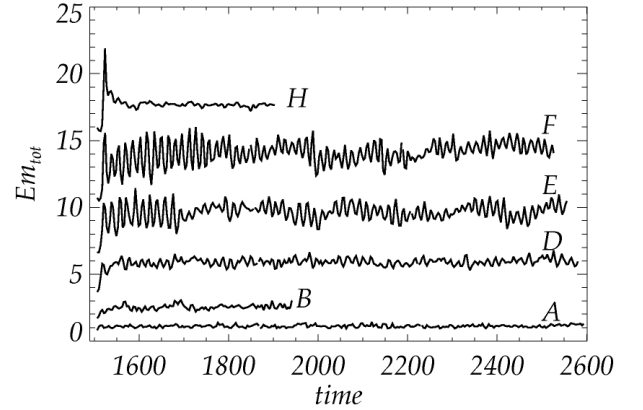


Fig. 2. Selected histories of magnetic energy for various runs, as indicated by the labels.

the model, i.e., size, location. The scales of density, gas pressure and temperature determine the state of matter. In order to perform the dimensional analysis, we need a standard solar model. In the current study, we adopt the combined model calculated by Guenther et al. (1992) (Table 3B therein).

In our thermally relaxed non-magnetic convection model, the input flux is ~ 0.065 , implying that the top of our box is at a depth of ~ 695 km from the solar surface (from unit continuum optical depth). This distance roughly corresponds to the depth of the Wilson depression.

The parameters of our models are summarized in Table 2.

For magnetoconvection it is in fact more meaningful to express magnetic field strength in terms of the *turbulent equipar-*

tion field rather than in Alfvénic units (or thermal equipartition field). The turbulent equipartition magnetic field B_e is defined by $\rho v^2/2 = B_e^2/8\pi$. We evaluate B_e at $z = 0.91$, near the top of the convectively unstable part but deep enough to be unaffected by the closed upper boundary condition. We find $B_e = 0.29B_{\text{sc1}} = 1025 \text{ G}$. Table 3 presents the strength of the imposed vertical magnetic field in the individual runs in units of B_e .

3. Numerical results and discussion

Upon starting the calculation with no magnetic field, after long term relaxation convection approaches a nearly steady state where the temporally and horizontally averaged total energy flux is nearly constant. The various contributions to the energy flux are shown in the upper left panel of Fig. 1. The strong downward directed kinetic energy flux is a well known hallmark of steady compressible convection, expected from convection theory (Unno & Kondo 1989; Petrovay 1990) and also consistent with numerical simulations (Chan & Sofia 1986). From the constancy of the total energy flux it is clear that the non-magnetic convection is completely relaxed.

Next, we superpose a vertical uniform magnetic field on an instantaneous snapshot of the relaxed non-magnetic convection. Fig. 2 shows the time history of magnetic energy for some of the cases listed in Table 3. It is apparent that after a short while, the magnetic energy contained in the system becomes statistically steady. For the cases with very weak or very strong fields, the relative fluctuation of the magnetic energy is lower than in the intermediate cases E and F. The reasons for this will be clarified below.

3.1. Flow morphology

The effects of a vertical magnetic field imposed on the granulation pattern are summarized in Fig. 3.

As revealed by previous studies, e.g., Weiss et al. (1996); Stein & Nordlund (2000), for low field strengths magnetic fields are intermittent, concentrated into flux tubes confined to the narrow lanes of the intergranular network (case A). For somewhat stronger fields the flux tubes join to form a connected network (case B). The suppression of motion in the area of strong magnetic fields is clearly seen.

In the opposite limit of very strong imposed magnetic field, convective flows are restricted to narrow columns separated by strongly magnetized, nearly stagnant fluid (case H). Each of these narrow columns consists of a single convective cell, seen in cross section in the figures. The size of these small scale convective elements is small compared to the sizes of normal granules, inviting comparison to the umbral dots observed in sunspots. This correspondence was indeed suggested by Weiss et al. (2002). Note, however, that the small scale convective elements in the experiments of Weiss et al. (2002) only contained upflows, their upwards directed mass flux being compensated by a slow sinking motion in the strongly magnetized bulk fluid. In contrast, we find strong localized downflows adjacent to the upflows, within the non-magnetic convective columns. This property makes our small scale convective elements a close relative of the *convectons* of Blanchflower (1999) and Blanchflower & Weiss (2002) so for brevity, in the following we will refer to them by this name.

In the intermediate cases E & F we recover the flux separation phenomenon, first discovered by Tao et al. (1998), where

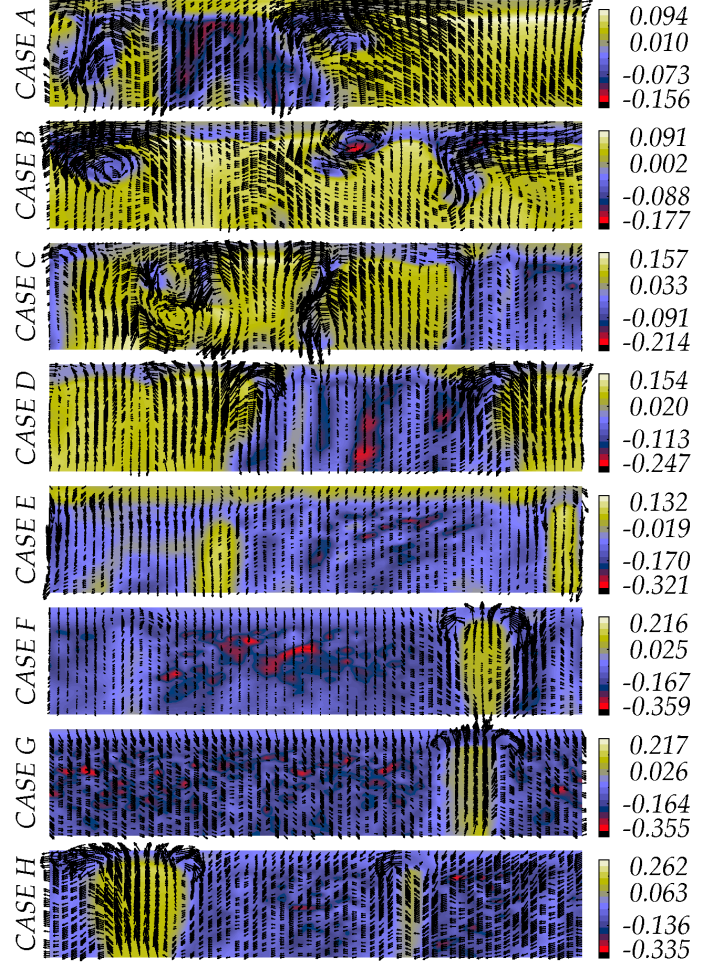


Fig. 4. A vertical cut of our box along $x = 2.5$ at an arbitrary instant. The colour scale represents temperature; vectors represent the velocity field projected on the plane. Rows correspond to different runs as labeled on the left.

small scale convection and vigorous granular convection coexist, the latter being present in large field free patches (in what follows: *inclusions*, for brevity) embedded in a strongly magnetized fluid displaying SSC in the form of scattered convectons. Each inclusion includes several granules. The size of the inclusions is comparable to the size of our box: it is this effect that leads to the large relative fluctuations of magnetic energy in cases E and F (Fig. 2).

Finally, the snapshot for case G in Fig. 3 displays multiply segmented convective plumes of size intermediate between inclusions and convectons. The lanes segmenting these elements are cool and coincide with downflows. This already suggests that our case G represents a heretofore unknown transitional regime of magnetoconvection between small scale convection (SSC) and fully developed flux separation (FXS) —a finding that will be corroborated below.

Figs. 4 and 5 present vertical cuts of our box. As expected, stronger magnetic field is generally associated with cooler gas —usually even cooler than in the less magnetized downflows. In the weak field cases, despite our imposed boundary conditions of a vertical magnetic field, the field lines often get quite tangled inside the convective region as the vigorous convective flows freely deform them. In the strong field case, on the other

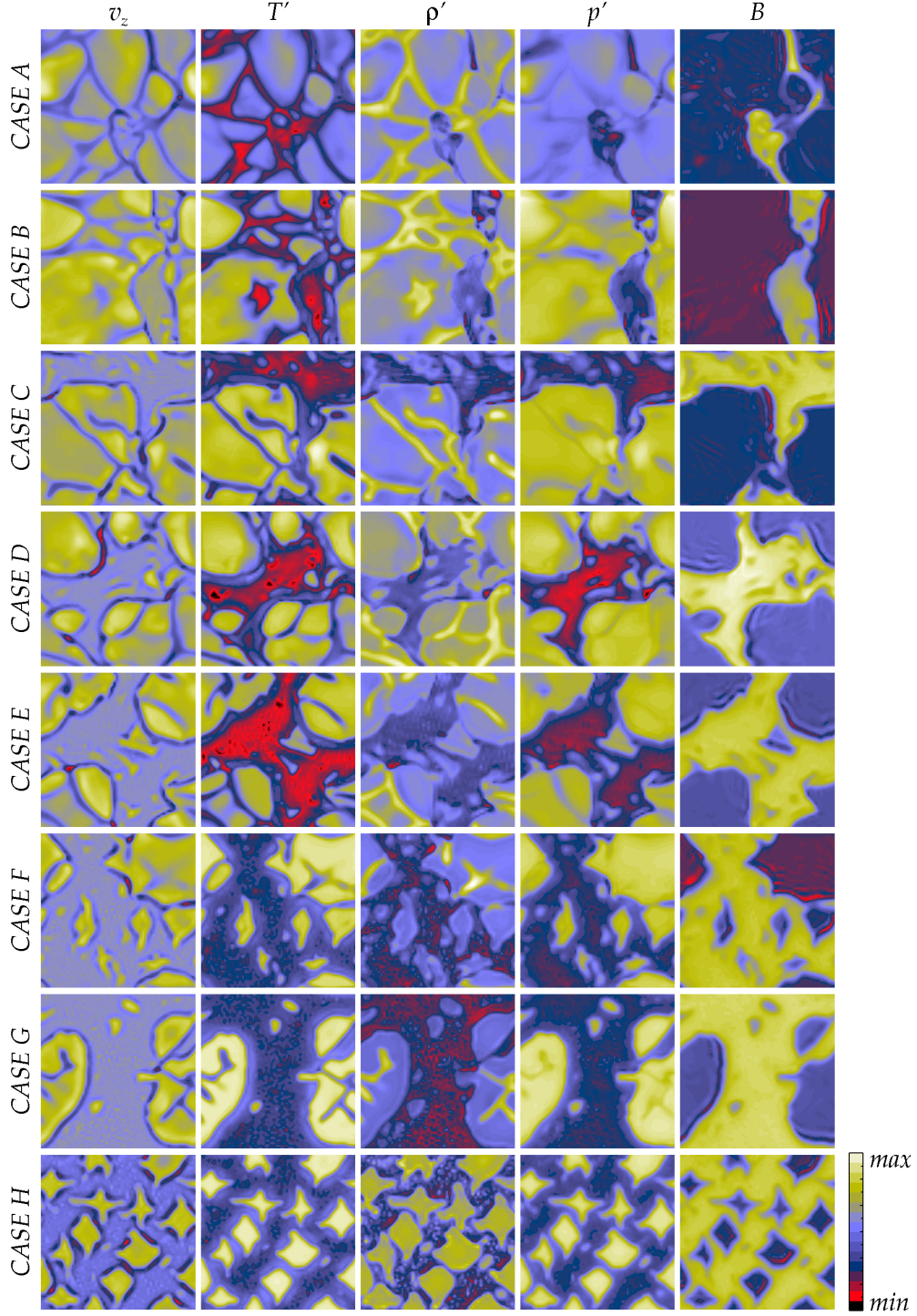


Fig. 3. Contour plots various physical quantities, as marked on top of each column, in a horizontal cut of our box at $z = 0.78$ at an arbitrary instant. Rows correspond to different runs as labeled on the left.

hand, field lines remain close to vertical and the columnar shape of convectons is apparent.

It is clear from these plots that the size of the various convective structures is not very small compared to the size of our box, leading to an imperfect cancellation of turbulent fluctuations. This results in significant temporal fluctuations of the total magnetic energy (cf. Fig. 2). Furthermore, momentum is not

conserved in our simulation as it can be advected in and out of the box through the open lower boundary. In many cases this results in a net uniform mean flow. Both effects are particularly strong in the flux separation cases (E and F), due to the presence of the inclusions with a size comparable to the domain size. In our plots of the velocity field the resulting mean flow has been subtracted for clarity. In a few runs made with larger box sizes

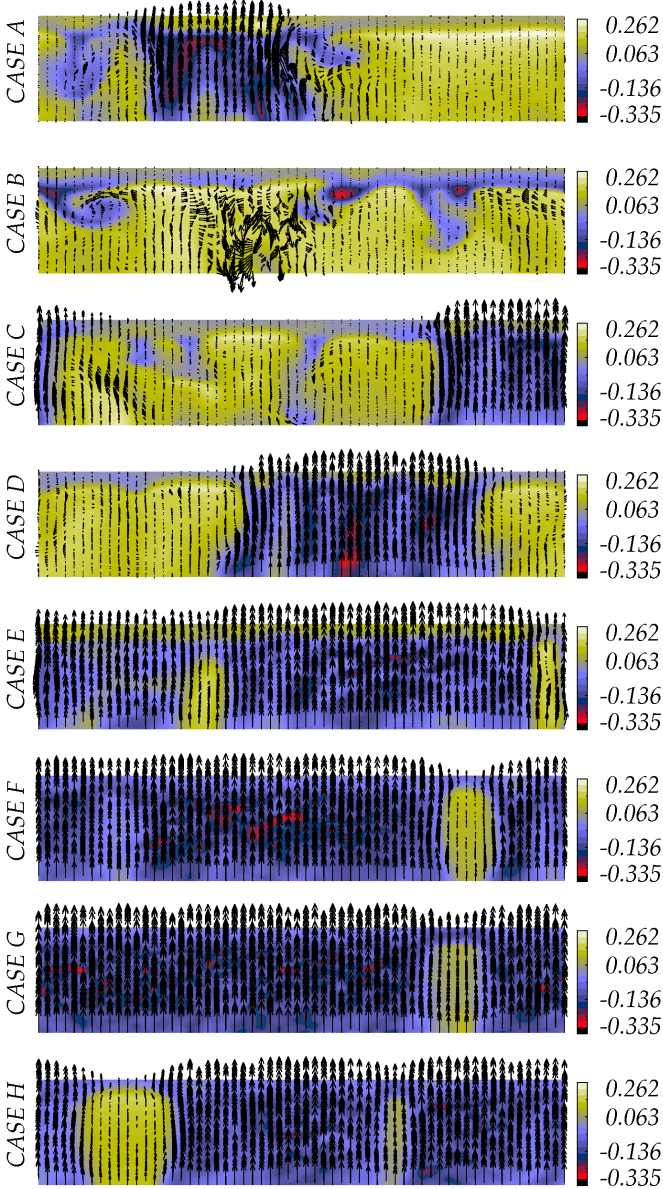


Fig. 5. Same as Fig. 4 except that vectors now represent the magnetic field.

and/or closed lower boundary we confirmed that the net horizontal flow indeed vanishes in these cases, while otherwise the results remain unchanged.

3.2. Time evolution

Fig. 6 and Fig. 7 illustrate the time evolution of vertical velocity and magnetic field strength near the top of the convective layer. The evolution is more clearly seen in the corresponding animations, publicly available at <http://astro.elte.hu/~kris/magconvmovies>

The convectons seen in the strong field case H are fairly persistent but they slowly pulsate. The small-scale convective motion is confined in thin vertical field-free columns. The cross section of these columns evolves with time periodically, as indicated by the small white box in first row of Fig. 6.

It is interesting to note that as the largest convectons approach their maximum size a downdraft often appears in their middle. The downdraft is obviously cooler and somewhat more magnetized than the rest of the convecton. This phenomenon is somewhat analogous to the first phase in the development of exploding granules as seen in quiet sun observations. In fact, this is but a first sign of the more spectacular temporal variation of the convective elements seen in case G.

The time variation of the convective elements in case G reveals a new type of behaviour apparently not seen in previous simulations. The pulsation of some convectons reaches an extremely high amplitude. During their size increase, multiple downdrafts appear inside them; then, these downdrafts merge into a network of internal downflow lanes, lending the convective element a segmented appearance, reminiscent of a granular inclusion. (Again, note the analogy with exploding granules, cf. Hirzberger et al. 1999.) What we see here is essentially convectons developing into inclusions and back, on a time scale much longer than the pulsation period of normal (small) convectons. (In dimensionless units, the cycle time is ~ 100 vs. ~ 20 .) Case G thus represents a hitherto unseen transitional state between small scale convection and flux separation.

In the flux separation case (E and F) we have normal granular convection going on inside the inclusions while small, fairly steady convectons can be observed in the magnetized fluid in between. There seems to be no more evolution of convectons to/from inclusions, though the possibility cannot be excluded that on time scales much longer than the length our run such evolution may still occur.

Finally, for even weaker fields the magnetized component becomes limited to a network of channels between the inclusions (case B), a patterns sometimes observed in plages or facular areas. These thin magnetized channels do not support small scale convection any more. For the weakest fields, the magnetic field becomes intermittent, breaking up into flux tubes confined to the intergranular lanes and defining a sort of “supergranular” network (case A).

3.3. Flow statistics

For a more quantitative analysis of the properties of turbulent magnetoconvection we plot the PDFs (probability distribution functions) of the vertical components of the magnetic field strength (in Alfvénic units) and of the flow velocity in Fig. 8 and Fig. 9, respectively. Only typical cases are plotted, i.e., SSC (case H), FXS (case E), and GRC with intermittent fields (case A). In Fig. 9 the non-magnetized convection case is also shown. The data are sampled at two horizontal layers: near the upper convective boundary ($z \sim 0.8$) and deep inside of the convective part ($z \sim 0.33$).

The shape of PDFs for the distribution of vertical Alfvénic speed is similar in both layers sampled. This might be due to the fact that our models are not very deep and subject to vertical field line boundary conditions. Overall, these PDFs are rather similar to those obtained by Weiss et al. (2002).

For SSC (case H, red dashed), the PDFs are relatively flat, with a smooth peak just below the maximum Va_z (magnetized component) and a sharp peak around 0.1 (convectons). In contrast to Weiss et al. (2002), in the current study the range of field strengths extends to negative values even when the imposed field is strong. This may be related to the presence of localized downdrafts adjacent to upflow plumes in convectons: the resulting strong rotational shear can play havoc with the field lines of

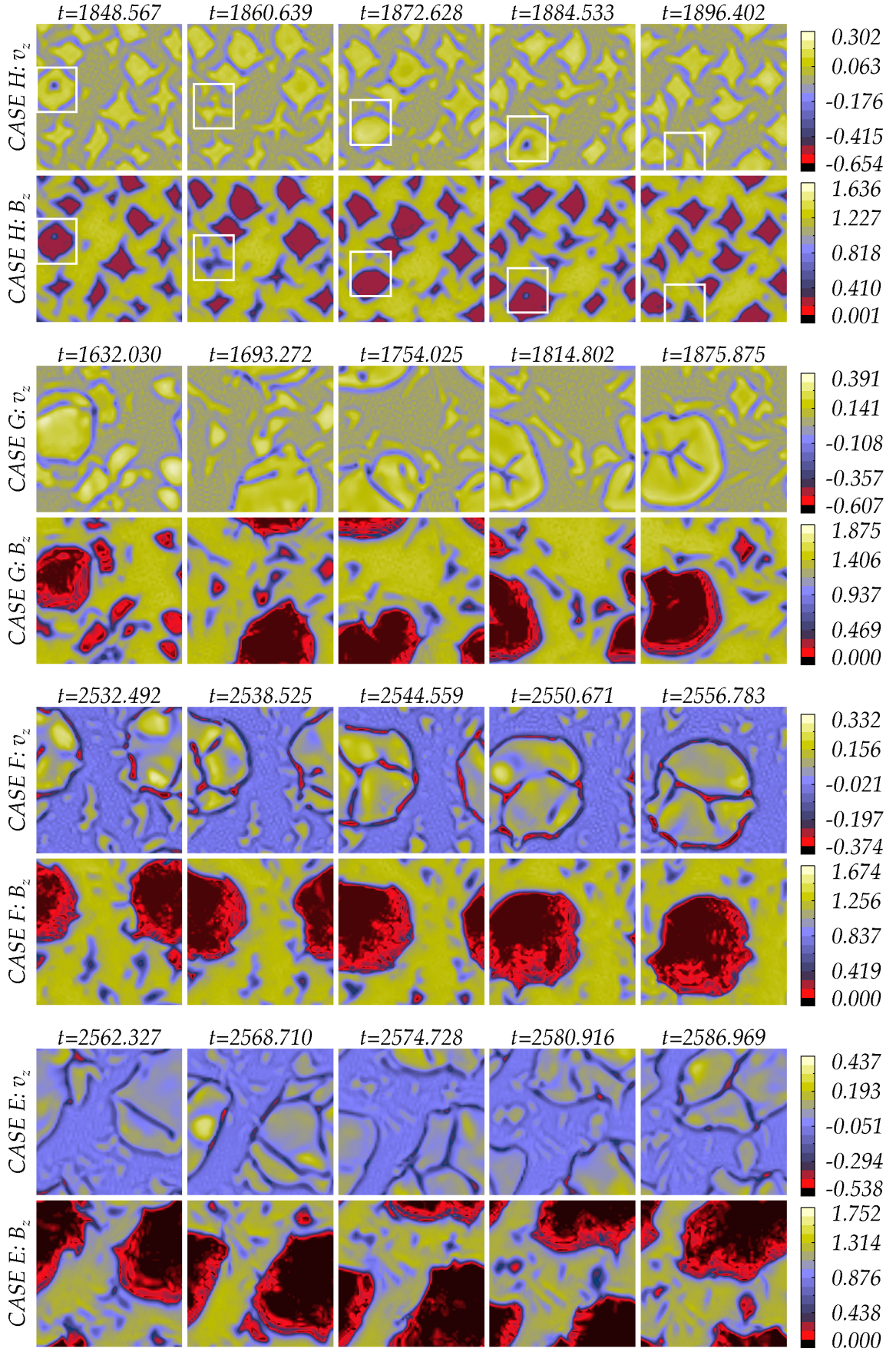


Fig. 6. Time evolution of vertical velocity (odd rows) and vertical magnetic field strength (even rows) at $z = 0.8$, near the top of the convective layer. Each pair of rows presents a different run as indicated by the labels. Cases H, G, F and E are shown. Note that in case G the time interval between the consecutive snapshots is significantly longer than in the other cases. For case H a white box encloses a pulsating convective tube.

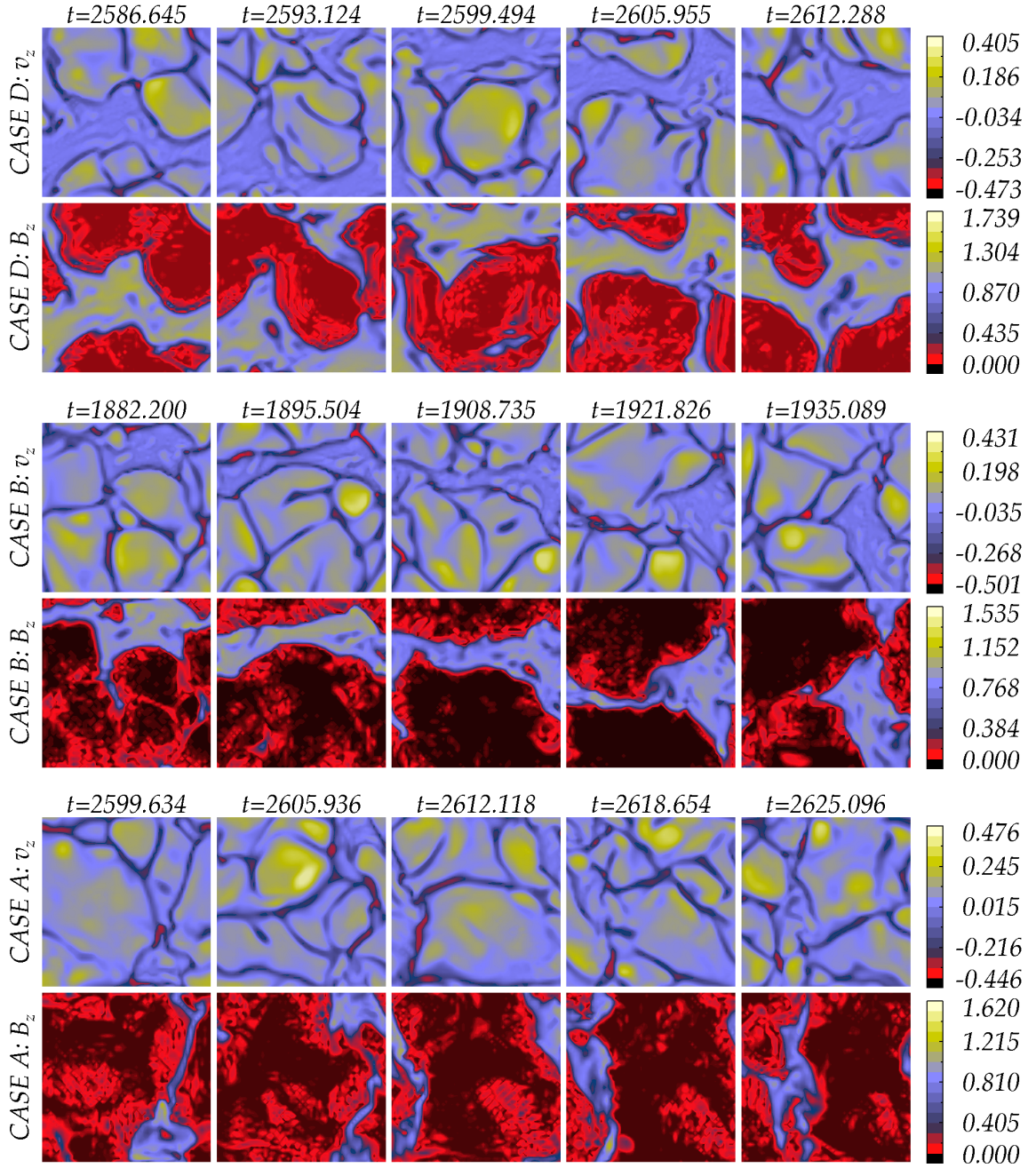


Fig. 7. Same as Fig. 6, for cases D, B and A

the weak magnetic field inside the convective column, occasionally turning around their vertical orientation.

For the intermittent field case with GRC (case B, black solid) the form of the PDF reflects turbulent flux expulsion, the symmetric peak around the origin corresponding to the weakly magnetized, vigorously convecting fluid while the smooth secondary peak at higher field strengths is due to the magnetic flux concentrations. This form of PDF is familiar both from previous simulations and from quiet sun observations (de Wijn et al. 2009).

For FXS, (case E, magenta dotted) the shape of the PDF is similar to case B but the strong field peak is higher and shifted towards higher field strengths, as expected.

Unlike the PDFs of the magnetic field strength, the PDFs of the flow velocity sampled in different layers show obvious discrepancies, as obvious from Fig. 9.

For GRC with intermittent magnetic field (case B, thick black solid), the PDFs of vertical velocity are almost identical to those of non-magnetized convection (thin blue solid). Their change of shape between the top and the middle of the convecting layer is related to the well known change of morphology from the observed granular pattern near the surface to isolated fast downdrafts embedded in a slowly rising, warm bulk fluid in the bulk of the convective zone. The lack of a clear secondary peak at negative velocities in the top panel may be due to the low filling factor of the downdrafts and possibly also to a lack of a characteristic scale among them.

As the imposed magnetic field is increased, the main peak of the PDFs shifts below zero. This indicates a general slow sinking of the magnetized fluid component. An extended shoulder on this peak on the negative side corresponds to the faster down-

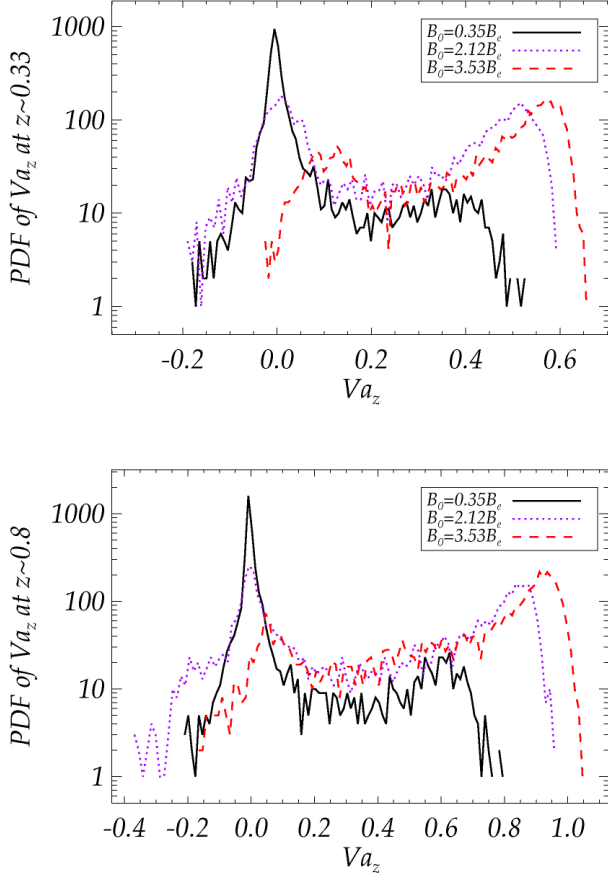


Fig. 8. PDFs for the distribution of vertical Alfvénic speed, $Va_z = B_z / \sqrt{4\pi\rho}$, at $z = 0.8$) and $z \sim 0.33$ for various imposed vertical magnetic field strengths as indicated inside the labels, corresponding to SSC (red dashed), FXS (magenta dotted) and GRC (black solid).

drafts localized next to the upflows. Both this shoulder and the secondary peak on the positive side representing the upflows are more distinct near the top of the convecting layer.

The anisotropy of turbulence is shown in Fig. 10. As expected, the ratio of vertical component to total field strength is approaching 1 as we increase the imposed magnetic fields (right hand panel). Even for the very weak field case, this ratio never goes below 0.9. This is simply because the field lines can only be significantly deflected from the imposed vertical direction in places where the magnetic field is inherently weak.

On the left hand panel the curves can be naturally grouped into three classes, according to their shape and position. These classes correspond to SSC (case H), FXS (E and F) and GRC with intermittent field (cases A–D). This lends more objective support for considering SSC, FXS and GRC three physically different modes of magnetoconvection. Furthermore, the curve representing case G (red dashes) is quite obviously a “hybrid”, its shape resembling case H but its overall position placing it in the FXS group. This, in turn, lends further support to our identification of case G as a new transitional mode between the SSC and FXS modes of magnetoconvection.

3.4. Comparison with observations

In the weakly magnetic cases the morphology, time dependence and statistics of our magnetoconvective flow is in good accor-

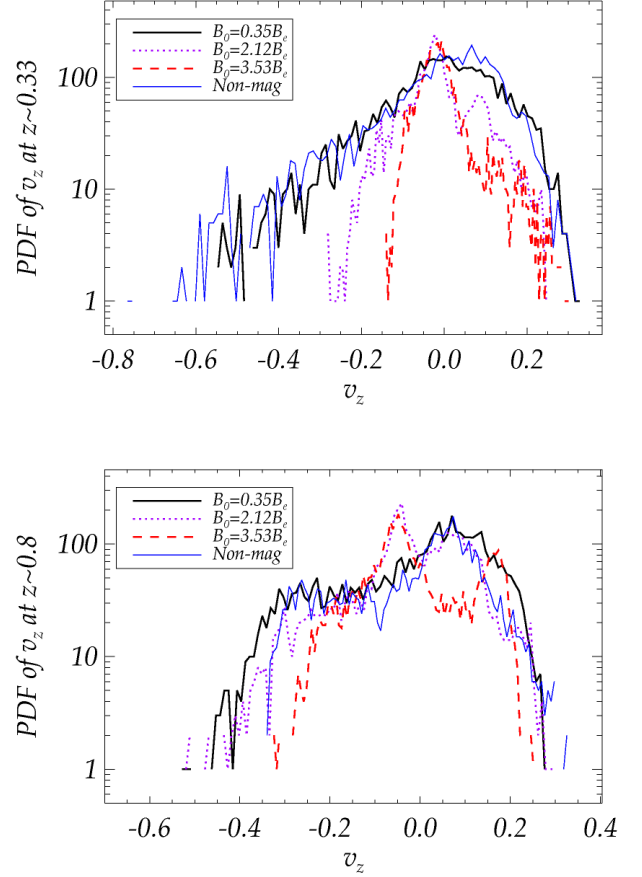


Fig. 9. PDFs for the distribution of vertical velocity, i.e., v_z , at $z = 0.8$) and $z \sim 0.33$ for various imposed vertical magnetic field strengths as indicated inside the labels, corresponding to SSC (red dashed), FXS (magenta dotted) and GRC (thick black solid). The blue thin solid thin is the PDF of the non-magnetized case.

dance with observations. This is so despite the fact that, when scaled back to physical units along the lines of Section 2.4, our convective structures are significantly larger and longer lived than those observed in the solar photosphere. We attribute this difference mainly to the lack of a freely radiating photosphere in our experiments, which is known to have a key role in determining granular scales (Rast 2003). The overall qualitative and quantitative similarity of the magnetoconvective structures in our weak field models to observations encourages us to look for similar observational parallels with the structures seen in our strong field experiments.

The analysis of high-resolution Dopplergrams and continuum images of sunspot umbrae by Bharti et al. (2007a) show that the umbral dots are surrounded by downflows. Localized downflows near UDs have also been observed by Ortiz et al. (2010). These observed umbral structures are quite similar in appearance to the convectons surrounded by a patchy ring of downflows, seen in our experiments in the SSC domain.

Furthermore, in larger umbral dots dark lanes are often observed. These UDs rarely have the regular “coffee bean” structure suggested by the simulations of Rempel et al. (2009b); instead, dark lanes are often asymmetrically positioned inside them, and multiple dark lanes are common, lending a segmented appearance to these UDs. Umbral dots with up to six dark lanes have been observed by Bharti et al. (2007b). Observations

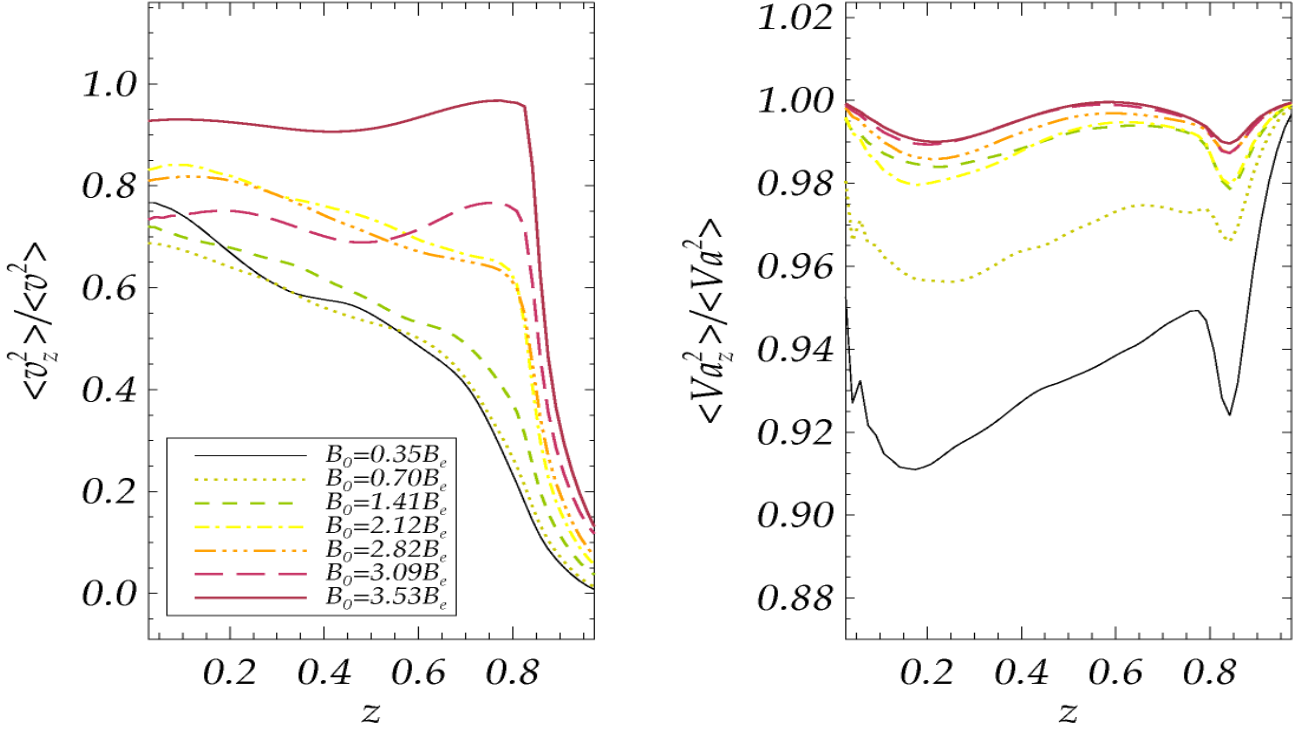


Fig. 10. Vertical anisotropy of the velocity field (left hand panel) and magnetic field (in Alfvénic units, right hand panel). for cases A (thin black solid), B (green dotted), D (green dashed), E (yellow dash-dot), F (orange dash–3dot), G (red long dashes) and H (red solid).

also indicate that the UD evolve rapidly compared to sunspots. Bharti et al. (2007b) showed how a UD with multiple dark lanes changed its appearance over the course of about an hour. (Note, however, that some of the apparent temporal variations in UDs may be due to seeing effects, cf. Hamedivafa 2011.)

These latter properties of UDs are more reminiscent of the transitional convective structures seen in our case G. Indeed, case G represents a vertical magnetic field strength of about 3 kG in physical units, just in the range expected for sunspot umbrae. We therefore suggest that conditions in sunspot umbrae correspond to the FXS-SSC (F/S for short) transitional regime identified in this paper.

4. Conclusion

We have constructed a series of numerical experiments of magnetoconvection in a layer of compressible plasma with an open lower boundary and bounded by a stable layer from above, using a BGK-MHD scheme. Our model setup differed from that of previous idealized magnetoconvection models (Weiss et al. 2002) in several important aspects, being closer to realistic solar conditions. Despite this, the general behaviour of the solutions as a function of the imposed field strength does basically agree with those models. In particular, flux separation (FXS) still prevails in a wide parameter range and the small scale convection (SSC) dominates the energy transport in the strong field case.

An important difference compared to the results of Weiss et al. (2002) is that in the SSC regime strong, narrow, patchy downflows appear in a ring around the narrow upflows in our experiments. Thus, our “convective columns” may be more closely related to the solitary “convectons” of Blanchflower & Weiss (2002) than to the localized plumes in previous magnetoconvection experiments. This property of our experiments is in agree-

ment with recent high resolution observations of sunspot umbrae (Bharti et al. 2007a; Bharti et al. 2009; Ortiz et al. 2010).

Furthermore, we have identified a hitherto unknown transitional regime between FXS and SSC. This F/S regime is very dynamic, with a continuous evolution of convectons into granular inclusions and back. Intermediate states of the convective elements are often reminiscent of larger, multisegmented umbral dots, also known to be subject to dynamic changes. This suggests that conditions in sunspot umbrae correspond to the F/S transitional regime identified in this paper and that UDs essentially represent convectons and/or convecton/inclusion transitional phases as seen in our run G.

It should be noted that the realistic numerical simulations of Schüssler & Vögler (2006) and Rempel et al. (2009b) suggest a somewhat different interpretation of the substructure and time dependence seen in UDs. The dark lanes in these simulations are due to an optical depth effect and they do not coincide with downflows; downflows, however, occur near the end points of the lanes. The finite lifetime of UDs, in turn is due to the “safety valve” mechanism operating at the magnetic cusp above the convecting columns, in a manner somewhat akin to the suggestion of Choudhuri (1986). High resolution observational studies of the correlation and relative position of downflows and dark lanes may help to clarify this issue in the future.

It should be added that while observations suggest that the properties of central umbral dots are different from those of peripheral umbral dots (Sobotka & Jurčák 2009), it is hard to draw a sharp line between the two groups and the finite tilt of the magnetic field may have an important role in determining the properties of central UDs as well. Non-vertical fields, e.g. due to a fanning out or twisting of the flux rope, may also be instrumental in inhibiting the appearance of flux separation inside sunspot umbrae —though this may be also explained simply by the strong

fields in sunspot umbrae or by the large depth (and consequently low aspect ratio) of the umbra.

These considerations suggest that one possible way to bring idealized models closer to realistic numerical simulations could be the extension of these results to the case when the imposed magnetic field is tilted.

Acknowledgements. The computations were tested and performed on Eötvös University's 416-core, 3.7 Tflop HPC cluster *Atlasz* and on the supercomputing network of the NIF Hungarian National Supercomputing Center (project ID: 1117 fragment). Support by the Hungarian Science Research Fund (OTKA grant no. K67746), by the European Commission's 6th Framework Programme (SOLAIRE Network, MTRN-CT-2006-035484) as well as by the European Union with the co-financing of the European Social Fund (grant no. TÁMOP-4.2.1/B-09/1/KMR-2010-0003) is gratefully acknowledged.

References

- Bharti, L., Beeck, B., & Schüssler, M. 2010, *A&A*, 510, A12+
- Bharti, L., Jain, R., & Jaaffrey, S. N. A. 2007a, *ApJ*, 665, L79
- Bharti, L., Joshi, C., & Jaaffrey, S. N. A. 2007b, *ApJ*, 669, L57
- Bharti, L., Joshi, C., Jaaffrey, S. N. A., & Jain, R. 2009, *MNRAS*, 393, 65
- Blanchflower, S. 1999, *Physics Letters A*, 261, 74
- Blanchflower, S. & Weiss, N. 2002, *Physics Letters A*, 294, 297
- Chan, K. L. & Sofia, S. 1986, *ApJ*, 307, 222
- Chandrasekhar, S. 1961, *Hydrodynamic and hydromagnetic stability* (Oxford: Clarendon Press)
- Choudhuri, A. R. 1986, *ApJ*, 302, 809
- de Wijn, A. G., Stenflo, J. O., Solanki, S. K., & Tsuneta, S. 2009, *Space Sci. Rev.*, 144, 275
- Guenther, D. B., Demarque, P., Kim, Y., & Pinsonneault, M. H. 1992, *ApJ*, 387, 372
- Hamedivafa, H. 2011, *Sol. Phys.*, 45
- Hirzberger, J., Bonet, J. A., Vázquez, M., & Hanslmeier, A. 1999, *ApJ*, 527, 405
- Houghton, S. M. & Bushby, P. J. 2010, *ArXiv e-prints*
- Kitai, R., Watanabe, H., Nakamura, T., et al. 2007, *PASJ*, 59, 585
- Moradi, H., Baldner, C., Birch, A. C., et al. 2010, *Sol. Phys.*, 267, 1
- Ortiz, A., Bellot Rubio, L. R., & Rouppe van der Voort, L. 2010, *ApJ*, 713, 1282
- Petrovay, K. 1990, *ApJ*, 362, 722
- Rast, M. P. 2003, *ApJ*, 597, 1200
- Rempel, M., Schüssler, M., Cameron, R. H., & Knölker, M. 2009a, *Science*, 325, 171
- Rempel, M., Schüssler, M., & Knölker, M. 2009b, *ApJ*, 691, 640
- Riethmüller, T. L., Solanki, S. K., & Lagg, A. 2008a, *ApJ*, 678, L157
- Riethmüller, T. L., Solanki, S. K., Zakharov, V., & Gandorfer, A. 2008b, *A&A*, 492, 233
- Rimmele, T. 2008, *ApJ*, 672, 684
- Schüssler, M. & Vögler, A. 2006, *ApJ*, 641, L73
- Sobotka, M. & Hanslmeier, A. 2005, *A&A*, 442, 323
- Sobotka, M. & Jurčák, J. 2009, *ApJ*, 694, 1080
- Sobotka, M. & Puschmann, K. G. 2009, *A&A*, 504, 575
- Stein, R. F. & Nordlund, Å. 2000, *Sol. Phys.*, 192, 91
- Tao, L., Proctor, M. R. E., & Weiss, N. O. 1998, *MNRAS*, 300, 907
- Tian, C. 2010, *ArXiv e-prints*=1010.3594
- Unno, W. & Kondo, M. 1989, *PASJ*, 41, 197
- Weiss, N. O., Brownjohn, D. P., Matthews, P. C., & Proctor, M. R. E. 1996, *MNRAS*, 283, 1153
- Weiss, N. O., Proctor, M. R. E., & Brownjohn, D. P. 2002, *MNRAS*, 337, 293